Delft University of Technology

Document Version
Final published version

Licence
CC BY

Citation (APA)
van Rooijen, N., Alonso Del Pino, M., & Llombart, N. (2026). Design of Near-Field Coupled Leaky-Wave Lens Antennas With Flat Interfaces for Material Characterization at Sub-THz Frequencies. *IEEE Journal of Microwaves*, *6*(3), 615 - 624. https://doi.org/10.1109/JMW.2026.3668936

IEEE Journal of
Microwaves

MTT-S
MHz to THz Community

Received 5 September 2025; revised 21 January 2026; accepted 20 February 2026. Date of publication 11 March 2026;
date of current version 7 May 2026.

Digital Object Identifier 10.1109/JMW.2026.3668936

Design of Near-Field Coupled Leaky-Wave Lens Antennas With Flat Interfaces for Material Characterization at Sub-THz Frequencies

NICK VAN ROOIJEN, MARIA ALONSO-DELPINO (Senior Member, IEEE), AND NURIA LLOMBART (Fellow, IEEE)

(Regular Paper)

Terahertz Sensing Group, Microelectronics Department, Delft University of Technology, 2628 CD Delft, The Netherland, s

CORRESPONDING AUTHOR: Nick Van Rooijen (e-mail: n.vanrooijen@tudelft.nl).

This work was supported by Huawei Technologies Sweden AB.

ABSTRACT This work describes the design of sub-Terahertz lens antennas that are coupled in the near field. The lenses have a flat interface, making them suitable for material characterization under plane wave incidence. A waveguide-based leaky-wave antenna feed illuminates the lenses efficiently with a Gaussian pattern over a bandwidth of 140 to 220 GHz. Then, a large permittivity hyperboloid lens converts the feed pattern into a plane wave with high Gaussicity. The use of dense dielectric materials significantly reduces field spreading effects when compared to setups with free-space propagation. Furthermore, the final lens architecture presents a flat interface, enabling direct lens-to-lens coupling for 2-port measurements with only −3 dB of coupling loss. This way, a quasi-optical Thru-Reflect-Line calibration can be performed, thereby making accurate extraction of material properties via full S-parameter matrix possible. Two materials were studied with this technique in a full-wave simulation, showcasing errors below 1 percent for permittivity and 2 percent for loss tangent, using a standard plane-wave propagation model.

INDEX TERMS Antennas, flat interface, material characterization, plane-wave generation, sub-THz, WR-5 waveguide.

I. INTRODUCTION

Material characterization in the sub-terahertz frequency spectrum presents promising new opportunities. Accurate, non-invasive material parameter extraction in this frequency band enables a variety of different applications, with examples including security, industrial material quality and defect detection, and air quality detection [1], [2], [3], [4]. Furthermore, accurate material characterization is key to designing and optimizing Radio Frequency (RF) systems, as their performances rely heavily on the properties of the involved materials. For these reasons, material characterization in these bands is met with growing interest, and a variety of different measurement techniques have been proposed.

At frequencies < 300 GHz, a popular approach is to use a Vector Network Analyzer (VNA) for material characterization. Here, frequency-domain S-parameter matrices are compared to an analytical model for extraction of complex permittivity values [5]. Rectangular waveguides in particular offer a controlled single-mode environment, in which a highly accurate Thru-Reflect-Line (TRL) calibration can be performed [6], [7], [8]. Unfortunately, the technique is no longer non-invasive, as the Material-Under-Test (MUT) needs to be adjusted to fit in the waveguide assembly. This becomes increasingly difficult at higher frequencies, where the waveguide dimensions are smaller. Free-space material characterization techniques are therefore preferred for their flexibility [9].

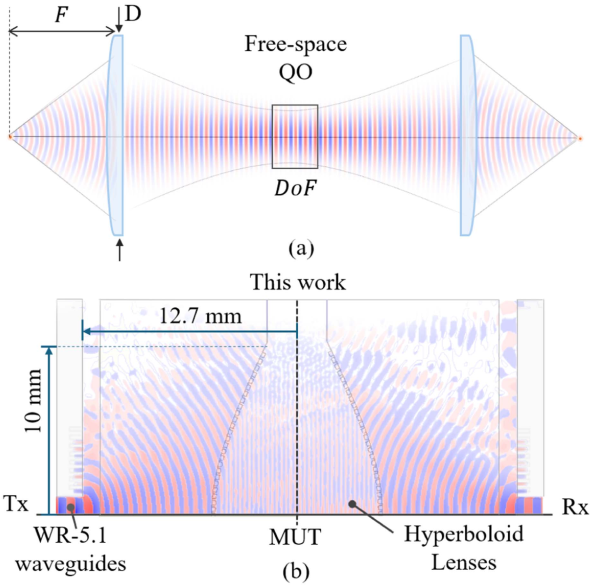

FIGURE 1. **(a) Conventional free-space quasi-optical approach using focused Gaussian beams, relying on a narrow Depth-of-Focus (DoF). (b) Proposed quasi-optical material characterization system. The Material-Under-Test (MUT) is positioned in between the two waveguide-fed hyperboloid lenses.**

Above frequencies of 300 GHz, a commonly encountered technique for free-space material characterization is terahertz Time-Domain Spectroscopy (TDS) [10], [11], [12], [13]. It uses a wide-bandwidth system to obtain the sample permittivity, by extracting the time-domain propagation delay through the sample. However, TDS systems do not provide full S-parameter matrices, and can therefore not be used in high-accuracy calibration techniques (e.g., TRL). Therefore, many recent works have explored sub-THz (100 - 300 GHz), VNA-based free-space measurement setups [2], [9], [14], [15], [16], [17], [18], [19].

However, contrary to the use of rectangular waveguides, in free-space measurement setups there is no well-defined mode with a single direction of propagation. This causes a limitation in accuracy when extracting the complex permittivity using analytical models, since they rely upon the assumption of a plane-wave incidence on the dielectric sample.

Therefore, efforts have generally focused on developing Quasi-Optical (QO) measurement setups, where the fields approximate the plane-wave condition using Gaussian beam optics [2], [9], [14], [15], [16], [17], [18], [19]. This well-known concept is illustrated in Fig. 1(a). However, the plane-wave condition is met only at the Gaussian beam waist for a limited Depth-of-Focus (DoF), where the phase front resembles a plane wave. Large F-number optics, which require careful alignment in position and orientation, are required to enlarge the DoF [20]. This in turn requires the QO system to trade off its compactness for a larger DoF.

To counteract these problems, recent efforts have also attempted to adapt the analytical models to include the field spreading effects [14], [17]. Nevertheless, the reliance on low field spreading conditions complicates the modeling and decreases the accuracy that such systems can achieve. In addition, the use of standard horn antennas required further calibration to account for the frequency dispersion of the phase-center [14]. Other works utilized highly-efficient leaky-wave antennas that generate plane-waves using elliptical lenses [21], and were experimentally found to be suitable for broadband material characterization [22]. Unfortunately, the alignment of MUT and antennas was challenging, and free-space spreading effects persisted.

To face these challenges, this work proposes a novel, compact, leaky-wave lens design with a flat interface, that directly generates a high-purity plane wave. Contrary to other works found in literature, the lens directly generates a high-purity plane wave in a dense dielectric medium with low amplitude spreading and low phase dispersion, compared to free-space propagation. This way, accurate free-space material characterization using a VNA in the WR-5 band (44 % bandwidth) can be achieved. The lens design is shown in Fig. 1(b), and consists of a low-loss $\varepsilon_r = 2.3$ dielectric, and a high density $\varepsilon_r = 9.3$ thermoplastic. The lenses can be mounted on a WR-5 waveguide, and are calibrated using an accurate TRL approach. We demonstrate the material characterization with a standard plane-wave model, placing no emphasis on additional compensation with analytical spreading models. Furthermore, the flat interface allows the MUT to be clamped in between the Tx and Rx antennas, thereby enabling a simple assembly and a reduction in angular misalignment.

This work is structured as follows. Section II provides an in-depth discussion on the used Gaussian propagation model, the design of the flat lenses. Then, Section III provides a full-wave simulation analysis of the designed lens, validating the claims made in Section II. Finally, Section IV describes the method to characterize materials using the established lens architecture, and two example cases are demonstrated.

II. LENS ANTENNA DESIGN

This section describes the design and modeling process for the lens architecture. It starts by modeling the electric field propagation using Gaussian beam theory. Then, the leaky-wave feed that illuminates the lens is analyzed, followed by the actual hyperboloid lens design.

A. GAUSSIAN BEAM PROPAGATION

In the first step, some a priori information on the Gaussian wave-front propagation is modeled. This helps us establish a relationship between the lens aperture dimensions and the MUT sample thickness.

As mentioned in the introduction, standard dielectric measurements rely on a transmission line model that assumes plane wave incidence. However, the generated plane wave will diverge as a function of distance, developing an increasingly large beam waist with a larger radius of phase-front curvature. MUT samples with large thickness can therefore suffer from increased electric field spreading and lower coupling.

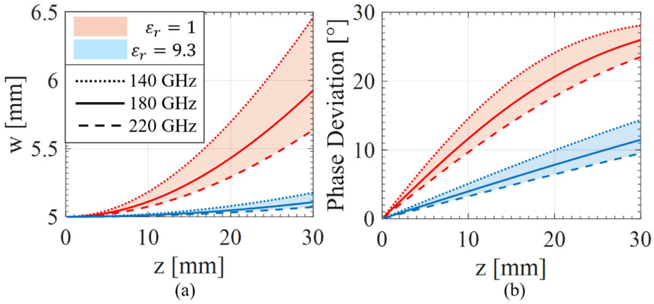

(a) (b)

FIGURE 2. **(a) Gaussian beam width w as a function of distance *z*. Two values for permittivity are indicated, plotted against the WR-5 frequency band. (b) The angular deviation from a plane wave, based on the radius of curvature.**

To assess the impact of such spreading effects, we model the field propagation using a standard Gaussian model [23]. First, the Gaussian beam width can be modeled using

$$w(z) = w_0 \sqrt{1 + \left(\frac{z\lambda_d}{\pi w_0^2}\right)^2}, \tag{1}$$

where λ_d is the wavelength in the dielectric medium, z is the propagation distance, and w_0 is the beam waist at $z = 0$. An example w_0 of 5 mm is used, corresponding to 3 λ_0 at 180 GHz. Similarly, the radius of curvature is calculated using [23]

$$R(z) = z + \frac{1}{z}\left(\frac{\pi w_0^2}{\lambda_d}\right)^2. \tag{2}$$

From the radius of curvature then follows the phase deviation from an ideal plane wave, defined by [24]

$$\Delta\Phi(x, y, z) = \frac{k_d \rho^2}{2R(z)}, \tag{3}$$

where k_d is the wave number in the dielectric medium and ρ defined as $\rho = \sqrt{x^2 + y^2}$.

Fig. 2(a) shows as an example the propagation of the Gaussian beam as a function of distance z, whereas Fig. 2(b) shows the phase deviation at $\rho = w_0 = 5$ mm. A frequency bandwidth of 140 GHz to 220 GHz is indicated. As expected, diffraction effects cause the initial plane-wave fronts to diverge, creating a widening of the beam width (Fig. 2(a)). The divergence also causes the wave-fronts to curve away from the central axis, causing increasing phase deviation to occur (Fig. 2(b)).

When comparing the spreading in vacuum ($\varepsilon_r = 1$) to that in our proposed ($\varepsilon_r = 9.3$) medium, the former presents a significantly larger spread over distance due to the factor $\sqrt{9.3}$ smaller electrical size of w_0. This is especially true for the lower frequency bound of the bandwidth (dashed line), where the beam width is electrically smaller.

Based on this modeled behavior, it is apparent that by confining the Gaussian beam within a medium of high ε_r, a significant decrease in spreading over distance can be achieved. The distance z can be connected to the maximum MUT thickness, by estimation of the number of multiple reflection required to reach convergence conditions. For example, $\varepsilon_r = 1$ samples with a thickness of 3mm can be analyzed with 26° phase deviation on the 5th back-and-forth reflection (total 30mm). By comparison, the denser $\varepsilon_r = 9.3$ reaches an 11° phase deviation over the same distance. The phase deviation can be further reduced by enlarging the lens D_L, thereby enlarging the Gaussian beam waist.

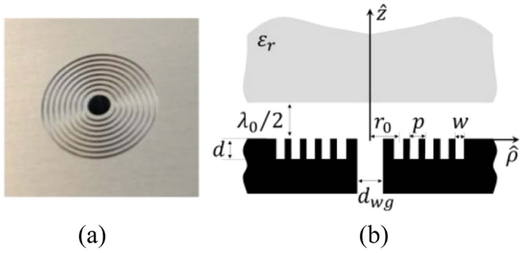

(a) (b)

FIGURE 3. **Elliptical lens antenna with leaky-wave feed, including a corrugated annular ring ground plane, taken from [21].**

B. LEAKY-WAVE FEEDING ANTENNA

The lens feed is of critical importance to the generation of the high-purity plane waves. Illumination of the two lenses requires a high degree of rotational symmetry and low cross-polarization levels (CX). The primary patterns should introduce an amplitude taper to avoid significant diffraction effects at the lens edges. In addition, for the generation of plane waves over a wide bandwidth, a near-constant phase center location is required. These already challenging properties must persist over a wide bandwidth, from 140 GHz to 220 GHz. Therefore, a specially designed feeding antenna is required that meets these criteria.

Fortunately, such a feeding antenna was developed in earlier work in [21], shown in Fig. 3. In that contribution, an elliptical ε_r=2.3 High-Density Polyethylene (HDPE) dielectric lens is positioned above an open-ended circular WR-5 waveguide. The two are separated by a $\lambda_0/2$ cavity. This structural combination enables the propagation of nearly-degenerate TM$_1$ and TE$_1$ leaky-wave modes. The non-dispersive TM$_0$, which is associated with high CX levels, was attenuated by the addition of circular corrugations around the waveguide. The result was an antenna feed that enables highly aperture efficient lens illumination, operating over the full WR-5 bandwidth (140 GHz to 220 GHz).

The feeding antenna was analyzed whilst radiating in an infinite HDPE medium, to obtain the feed performance. Fig. 4(a) shows the normalized amplitude patterns of such a feeding antenna. Indicated are the central frequency, and the lower- and upper-bounds of the WR-5 bandwidth. Its normalized E-fields are amplitude tapered towards a level of around −20 dB at 40°. Similarly, Fig. 4(b) shows the phase stability of the feeding antenna as a function of observation angle θ. Up to $\theta = 30°$, the phase ϕ remains constant between $-25° < \phi < 15°$. Beyond $\theta = 30°$, the amplitude tapering of Fig. 4(a) avoids the large impact of phase deviations on lens

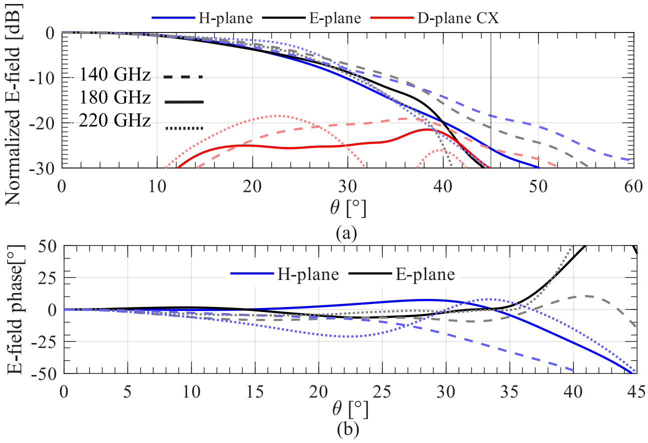

(a)

(b)

FIGURE 4. **Simulated primary patterns of the corrugated circular waveguide with leaky-wave feed of [21]. (a) The normalized far-field amplitude distribution for the E- and H-planes, including the D-plane cross polarization. Three frequencies are included representing the WR-5 bandwidth. (b) The phase distribution using the same nomenclature as (a).**

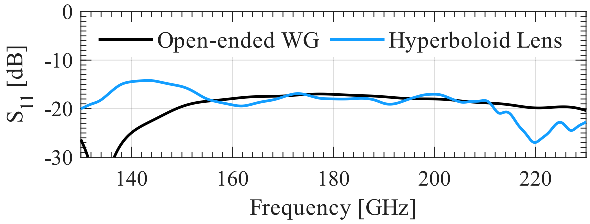

FIGURE 5. **Simulated S_{11} of the open-ended corrugated waveguide of [21], compared to the proposed hyperboloid lens. Both S_{11} curves are normalized to the waveguide characteristic impedance ($Z_c = 456\,\Omega$).**

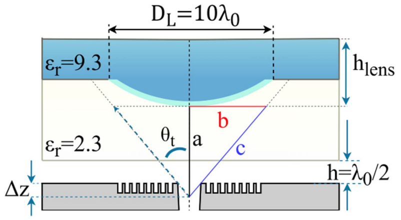

FIGURE 6. **Geometry of the lens with flat interface. In blue, the convex hyperboloid lens is made of dense thermoplastics. Below, the HDPE concave lens that supports the leaky-wave propagations in its air-filled cavity. The matching layer is located in between, indicated in cyan.**

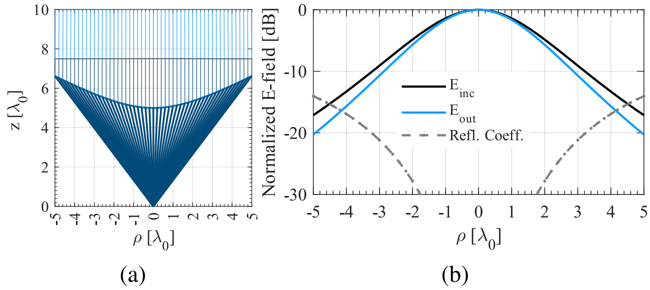

(a)

(b)

FIGURE 7. **(a) Ray tracing for the hyperboloid lens. The rays emanate from the phase center at $z = 0$. (b) Incident E-field amplitudes at the hyperboloid surface E_{inc} and at the flat lens-air interface E_{out}. The reflection coefficient is indicated in dashed lines.**

performance. Finally, the feeding antenna features a low S_{11} reflection parameter over bandwidth. The result is shown in Fig. 5. The low S_{11} is key to reducing multiple reflections in the lens setup.

C. HYPERBOLOID FLAT LENS DESIGN

Based on the knowledge of the feeding antennas and the Gaussian beam model, a lens architecture with a flat interface could now be designed. Given the $\varepsilon_r = 2.3$ of the leaky-wave feed, the second material made of $\varepsilon_r = 9.3$ PREPERM PPE950 thermoplastic was chosen for two reasons. First, the material was well characterized at high frequencies in [22], with a loss tangent $\tan\delta = 0.005$ at the WR-5 frequency band. Second, the material offers a good contrast from the HPDE, which is needed to refract the RF wavefronts whilst limiting the lens curvature. Limiting this curvature helps in implementing a matching layer later on.

Once the material selection was made, the lens topology was based on the available feed pattern and the flat interface requirement. Because the wavefronts travel from an $\varepsilon_r = 2.3$ to a more dense $\varepsilon_r = 9.3$ material, a transition towards a convex lens was required. Canonical hyperboloid lenses are a well-known type of lens to convert an incoming Gaussian radiation profile to parallel rays, e.g. a plane wave. The proposed lens architecture is shown in Fig. 6. The convex hyperboloid $\varepsilon_r = 9.3$ lens is positioned inside a concave cavity of the $\varepsilon_r = 2.3$ HDPE lens.

To suppress multiple reflections within the lens design, a Matching Layer (ML) is introduced between the interfaces of the two lenses. The same $\varepsilon_r = 4.6$ synthesized material will be used as in [22]. In this work, we assume the ML is made of a homogeneous material with a thickness of $\lambda_m/4$, where λ_m is the wavelength in the matching layer.

The hyperboloid lens topology can be modeled using standard hyperbola equations. The degree of lens curvature is determined by the material eccentricity $e_c = \sqrt{e_{r2}/e_{r1}}$, which is a function of the ratio of permittivities between the two mediums.

The lens is parameterized using its lens truncation angle θ_t and diameter $D_{:}$. Angle $\theta_t = 45^\circ$ was chosen to capture the feed primary patterns with sufficient spillover efficiency, whilst including a large amplitude taper to diminish diffraction effects at the lens edges (Fig. 4). Then, a lens diameter $D_L = 10\lambda_0$ was chosen to have the same 10 mm waist as was analyzed before, and to provide a good trade-off between lens thickness and aperture size. For structural strength, a sufficiently large $h_{\text{lens}} = 4.16$ mm $(2.5\lambda_0)$ was needed, as the PPE950 material can flex under mechanical stress.

After the lenses satisfy the above mathematical conditions using the stated geometrical parameters, a ray tracing approach can be implemented to confirm that the feeding rays refract to parallel outgoing rays. Fig. 7(a) shows the ray tracing simulation, where the rays emanate from the hyperboloid lens phase center at $z = 0$. A collimated beam is the result. Using the same technique, the phase errors across the $\varepsilon_r = 4.6$ matching layer were analyzed. The layer has uniform thickness, and therefore does not provide the same $\lambda_m/4$ condition for all angles θ. Using a simple ray tracing approach that compares the path length differences between rays at the central axis and at $\theta = 30^\circ$, such errors were found to be limited to 6.1°, 7.85° and 9.6° for 140, 180 and 220 GHz, respectively.

Fig. 7(b) shows the E-field amplitudes at the lens aperture. For simplicity, the feed patterns are fitted using a simple $E_{inc}(\theta) = cos^{6.5}(\theta)$ power distribution to match the tapering of the leaky-wave feed at the specified truncation angle θ_t, see Fig. 4.

III. FULL-WAVE SIMULATIONS

So far, theoretical models have been used to shape the lens design. However, such models do not, for instance, take into account the multiple reflections that occur inside the lens antennas. Such reflections might no longer satisfy the plane-wave based analytical models and therefore require time-gating to improve the accuracy of the lens setup.

Therefore, for a complete picture, full-wave simulations were performed by exporting the lens geometry to CST Microwave Studio. For the simulation, a homogeneous matching layer with $\varepsilon_r = 4.6$ is considered. All simulations include dielectric and ohmic losses. For aluminum, a conductivity of $\sigma = 4 \times 10^7$ Sv/m was used. The HDPE has a loss tangent of 3.3×10^{-4}, and finally the PREPERM is given a loss tangent of 5×10^{-3}.

A. STANDALONE LENS

First, we simulate the lens as a standalone element, radiating inside a semi-infinite $\varepsilon_r = 9.3$ medium. Open-boundary conditions were established at the outer edges to avoid reflections in the simulation box.

Fig. 5 includes the full-wave simulated S_{11} of the lens under the above-mentioned conditions. Because the matching layer provides a good anti-reflection layer, a similar S_{11} behavior is obtained when compared to the feeding antenna of [21]. At 140 GHz, the reflection coefficient is increased to -15dB. Most likely, this is where the $\lambda_m/4$ condition is not sufficiently met. A broader band unit-cell design of the matching layer [25] could help resolve the issue.

The normalized E-field at 180 GHz is shown in dB in Fig. 8. The top half represents the H-plane, whereas the bottom half is the E-plane propagation (symmetry planes were used). The planar wavefronts are clearly visible. The E-plane has slightly higher spillover loss, caused by the asymmetry in the primary pattern (Fig. 4).

To quantify the E-field quality on the lens interface at z = 12.5 mm of Fig. 8, the amplitude and phase distribution is shown in Fig. 9. The E-field amplitude matches well to that of the modeled E_{out} of Fig. 7(b), with amplitude asymmetries up to 1 dB at 30 ° incidence angle, as expected from the feed pattern of Fig. 4. The phase remains stable within 40° from broadside within the beam waist. Such phase distortions arise from both the feed pattern and length differences over angle θ in the uniform matching layer.

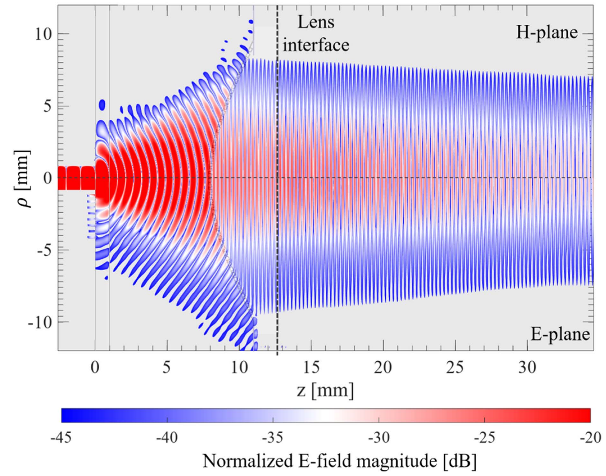

FIGURE 8. Simulated $\Re|E|$ propagating in the H-plane (top half) and E-plane (bottom half) at 180 GHz.

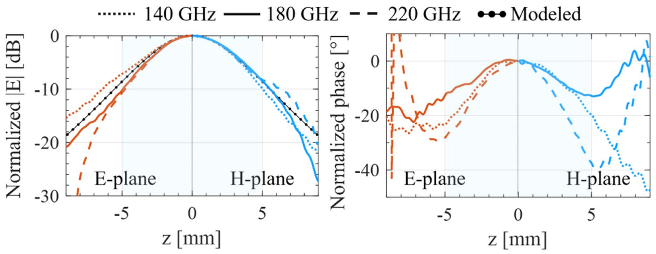

(a) (b)

FIGURE 9. Simulated normalized E-field (a) amplitude and (b) phase distributions across the lens aperture at z = 12.5 mm of Fig. 8. The E-planes (left halves) and H-planes (right halves) of both figures are compared over the frequency bandwidth. In (a), the modeled amplitude distribution of Fig. 7(b) is included for comparison. The shaded blue region represents the beam-waist at 180 GHz.

To assess the impact of the feed assymetries or deviations from the ideal Gaussian, we evaluate the Gaussicity $\eta_G(z)$ over distance, as in [18]. This metric is defined as the overlap integral between the actual E-field and an ideal fitted Gaussian beam over all the planes.

$$\eta_G(z) = \frac{\left|\int E_{\text{co}}(x, y, z)\, E_{\text{Gauss}}(x, y, z)\, dx\, dy\right|^2}{\int |E(x, y, z)|^2\, dx\, dy \cdot \int |E_{\text{Gauss}}(x, y, z)|^2\, dx\, dy}, \tag{4}$$

where $E_{co}(x, y, z)$ is the co-polarized E-field under test, $E(x, y, z)$ is the total E-field (including cross-polarization) and E_{Gauss} is the fitted ideal Gaussian E-field, defined using

$$E_{\text{Gauss}}(x, y, z) = A \cdot \exp\left(-\frac{\rho^2}{w_0(z)^2}\right). \tag{5}$$

The fitting is obtained by minimizing the error function, defined as the amplitude difference $|E_{\text{co}}|$ and $|E_{\text{Gauss}}|$. Amplitude

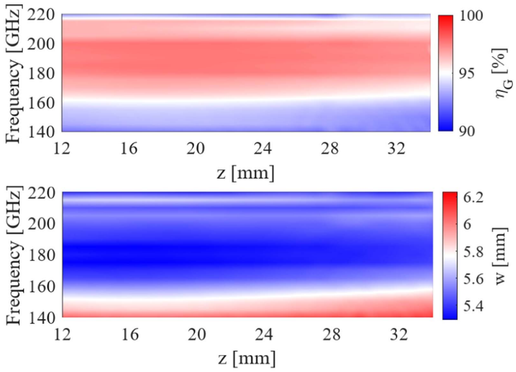

FIGURE 10. **(a) Simulated Gaussian efficiency in % of the E-field propagating along the *z* direction, evaluated across the WR-5 band. (b) The Gaussian beam waist w, fitted to the E-field data, as a function of propagation distance *z* for various frequencies.**

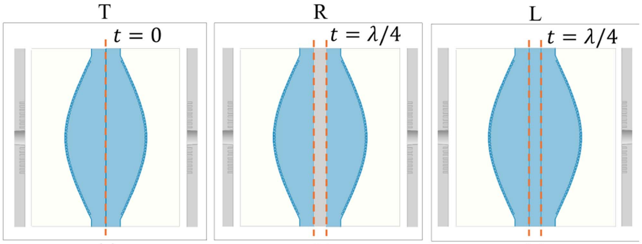

(a) (b) (c)

FIGURE 11. **T (a) -R (b) -L (c) calibration procedure for the lens-to-lens coupled antennas. In (b), a metal plate has been added in between the reference planes, separated by distance *t*.**

A is a normalization constant at $\rho = 0$. The beam waist $w_0(z)$ is fitted per distance z.

Fig. 10(a) shows the evaluated $\eta_G(z)$ as a function of distance, sampled uniformly over the WR-5 bandwidth. As expected, the frequencies outside the 160-215 GHz range have worst $\eta_G(z)$, attributed to the phase errors from the feed (up to 25 ° phase error), matching layer path length errors (max 9.6 °). The truncation effects will be limited, since the lens was tapered at -20dB amplitude levels. The frequency band from 160 to 215 GHz shows $\eta_G(z) > 95\%$, with a peak value of 97.7 % at 200 GHz. As was expected from the Gaussian beam modeling of Section II II-A, the Gaussicity does not decay very rapidly over distance, implying that the use of thick MUT samples is justified without large loss of accuracy. Fig. 10(b) shows the fitted Gaussian beam waist, indicating that the field does not significantly spread over distance, in accordance to Fig. 2.

B. TRL CALIBRATION SET

The final full-wave simulations are a set of Thru-Reflect-Line instances, shown in Fig. 11. These were simulated to extract the 2-port S-parameter boxes. For the Reflect, a Perfect Electric Conductor (PEC) plate was inserted between the Tx and Rx antennas. The Line has an added $\varepsilon_r = 9.3$, $\tan\delta = 5 \times 10^{-3}$, 90 ° phase shift transmission line, compared to the direct connection of the Thru. The dielectric line has a mesh cell size of $\lambda/40$, where λ is the wavelength in the associated medium, for a phase resolution of around 9°.

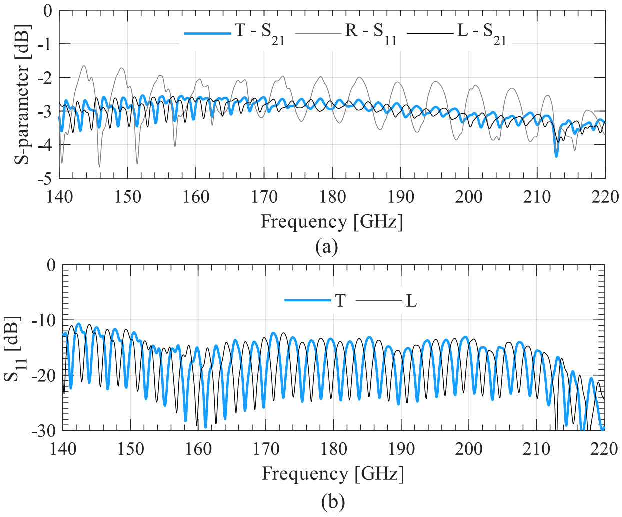

(a)

(b)

FIGURE 12. **Full-wave simulated S-parameters for the TRL simulations. Losses have been included. In (a) the (self) coupling between the different TRL components. In (b), the S_{11} parameters for the Thru and Line components.**

We first look at the simulated (self) coupling of the three components, shown in Fig. 11(b). A roughly -3 dB coupling is achieved for both the Thru and Line components. Dielectric losses in the PPE950 are a significant part of this, with a total dielectric loss of 2.2 dB (1.1 dB per lens). A different material for the convex lenses, such as alumina, could further improve coupling. The E-field propagation through the lenses was also visualized in Fig. 1(b).

The simulated reflection coefficients of the Thru and Line components are shown in Fig. 11(a). Both calibration standards maintain a $<$ 10dB S_{11}, even when coupled directly in the near field. Compared to Fig. 5, some higher-order ripples can be observed. However, due to the wideband lens design, these can be filtered out using time gating techniques. This topic will be further addressed in Section IV.

IV. MATERIAL CHARACTERIZATION USING THE LENS SETUP

The simulations of Section III-B provided a set of three 2-port S-parameters; S^{T}, S^{R}, S^{L}, for the Thru, Line, and Reflect, respectively, shown in Fig. 12. With these S-parameters, we can now de-embed the lens setup from an MUT, positioned between the reference planes shown in Fig. 11. This de-embedding is done using the TRL algorithm explained in [26], [27]. Once de-embedded, the material characteristics can be extracted.

In this work, the relative permeability (μ_r) of all materials is assumed to be 1 (i.e. non-magnetic). We electromagnetically characterize the MUTs by their complex relative

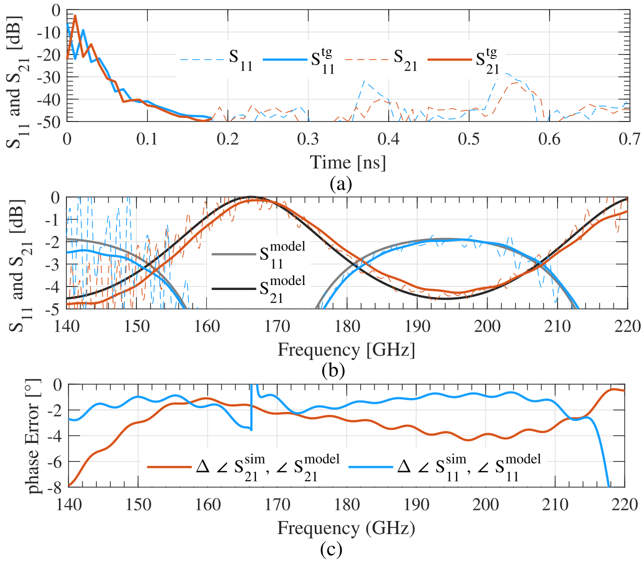

FIGURE 13. Simulated S-parameters of the case with vacuum in between the reference planes. (a) The time-response of S_{11} and S_{21} . The time-gated values are extracted from 0ns to 0.18 ns. (b) The resulting time-gated frequency domain S-parameters, compared to the transmission-line model. (c) resulting phase errors between the model and the simulated S-parameters.

permittivity $\varepsilon_r = \varepsilon_r' - j\varepsilon_r''$, where ε_r' is the real component of the permittivity and ε_r'' is associated with the dielectric loss. Both terms allow for the calculation of the dielectric loss tangent, obtained using $\tan\delta = \varepsilon_r''/\varepsilon_r'$. The analytical model used to fit the measured S-parameters to is explained in Appendix A. This section demonstrates the validity of the method using the dual-antenna setup using two simulated example cases.

A. CASE I: VACUUM

The first case investigates material characterization, where the MUT is a 2.7 mm thick slab of vacuum. The TRL of section III-B is applied to the simulated S-parameters, resulting in S^{sim}. By doing so, the reference planes are shifted to the MUT boundaries.

Fig. 13(a) shows the resulting S_{11}^{sim} and S_{21}^{sim} parameters in time-domain. Beyond 0.3ns, multiple reflections with an amplitude of at most -29dB are visible. However, due to the large frequency bandwidth (80 GHz) of the antenna, such reflections can be time-gated out, as indicated in Fig. 13(a). The time gate is applied from 0ns to 0.18ns.

This time-gating affects the frequency-domain S-parameters, shown in Fig. 13(b), by eliminating the ripples caused by the multiple reflections. The resulting $S_{11}^{\mathrm{sim,tg}}$ and $S_{21}^{\mathrm{sim,tg}}$ can then be compared to the S_{11}^{model} and S_{21}^{model} of (7) and (8), respectively.

As presented in (9), this comparison for the objective function is performed in both amplitude and phase, and therefore, Fig. 13(c) shows the simulated phase differences between $S^{\mathrm{sim,tg}}$ and S^{model} . As shown, the phase errors are limited to around -4° within the 150 to 210 GHz band. Outside this band, the error is larger, possibly caused by the decay in Gaussicity (Fig. 10), the increased S_{11}, or the ringing effects of the time-gating at the edges of the frequency bandwidth. Finally, as visible in Fig. 13(c), the phase of the $S_{11}^{\mathrm{sim,tg}}$ shows erratic behavior when $|S_{11}^{\mathrm{sim,tg}}|$ is going to zero at $\lambda_0/4$ multiples of material thickness. For this reason, the weight factor has been introduced in (9) to suppress erroneous fitting.

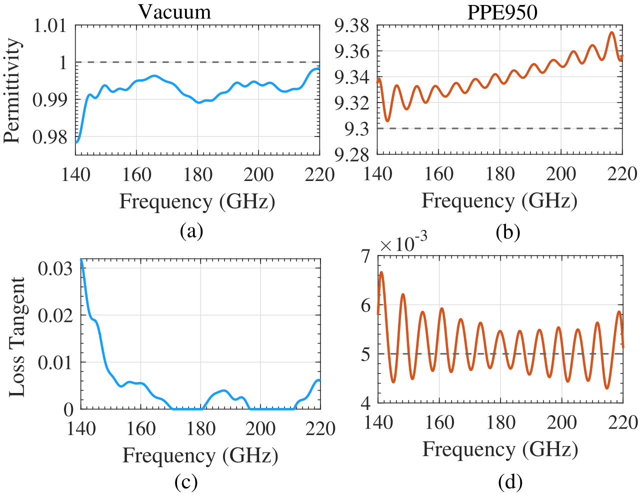

FIGURE 14. Simulated extracted material characteristics in terms of permittivity (a, b) and loss tangent (c, d). Two MUTs were characterized: vacuum (a, c) and PPE950 (b, d). Dashed horizontal lines indicate the true simulated values.

The post-processed $S^{\mathrm{sim,tg}}$ can then be used to extract the material parameters. Fig. 14(a), (c) shows the resulting permittivity (top) and loss tangent (bottom) for the analyzed vacuum material. For the permittivity, a roughly 1% error is made. The loss tangent is more difficult for low loss and electrically thin materials, and therefore suffers from larger errors.

B. CASE II: REFLECTIONLESS SLAB

The second case involves the characterization of a layer of 2.7 mm thick PPE950, with true permittivity of 9.3 and loss tangent of 5×10^{-3}. The same TRL and post-processing (including time-gating) procedure as in Section IV-A is performed. The calibrated S_{21} is shown in Fig. 15(a), and compared to the model, showing good agreement, apart from some remaining oscillations. Fig. 15(b) shows the phase deviation, indicating a drifting phase error of up to $+10^\circ$. The calibrated S_{11} is below -50dB due to the reflection-less interface. This verifies that the TRL has worked well, since the S_{11} from the antenna setup has been successfully de-embedded. For this reason, the transmission line model relies purely on the S_{21} for characterizing the material, since the weight w_Γ will be approximately zero.

Fig. 14(b) and (d) show the extracted material parameters. The permittivity is retrieved within a 0.8% error, and

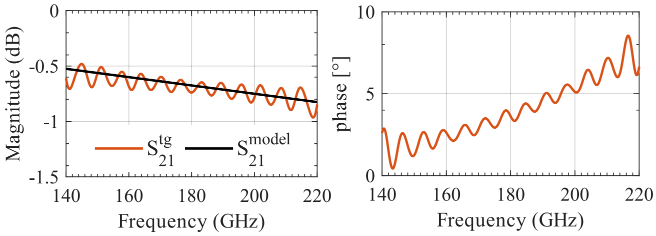

FIGURE 15. Simulated S-parameters of the slab of PPE950 material, calibrated and time-gated until its reference planes. (a) The time-gated frequency domain S-parameters, compared to the transmission-line model. (b) resulting phase errors between the model and the simulated S-parameters.

is slowly drifting due to the drifting phase error. The loss tangent oscillates around 5.1×10^{-3} with a standard deviation of 1.4×10^{-3} (2% mean error).

C. DISCUSSION

While these two cases demonstrate the promising antenna concept for material characterization, some notes on accuracy limitations in real-life implementation are necessary for completeness. First, the antennas will be fabricated with 100 μm ($\lambda_0/16$) tolerancing, presenting an upper-bound of 22.5° phase uncertainty. However, with sufficient SNR, such errors could be calibrated out using the TRL approach. Another source of potential error is that the method relies on the knowledge of the host material PPE950 permittivity. Calibration using an accurately known reference as a DUT is required to extract this permittivity. Finally, while MUT alignment errors are largely mitigated due to the flat interfaces of the antennas, the method assumes that the MUT is homogeneous in permittivity over the antenna aperture.

V. CONCLUSION

This work proposed a new lens architecture for high-frequency material characterization purposes, using the direct generation of high-purity plane waves. The plane wave propagates in a dense dielectric material, thereby significantly suppressing the field spreading effects, when compared to standard free-space setups. The lens structure offers a flat interface that offers great benefits when considering material measurements, as samples can be clamped between the lens interfaces.

Using a full-wave simulation approach, direct plane-wave generation was found to have a Gaussicity of > 94 % was achieved from 160 GHz to 215 GHz. A high port-to-port coupling of up to -3dB was achieved. The wideband antenna properties allow the usage of time-gating techniques to mitigate the impact of multiple reflections.

Using a TRL calibration technique, the reference planes can be shifted to the interfaces of the material under test. From there, the material complex permittivity can be extracted using a transmission line technique. This was exemplified in simulation two case studies, where the resulting errors were limited to 2% in permittivity and 2% in mean loss tangent.

The lens design could also enable applications in other fields, such as near-field telecommunications. The promising design and numerical validation of the proposed concepts opens the path for prototyping of this idea and performing experimental measurement of different samples.

Future improvements include further increasing the Gaussicity by shaping the lens design to better fit the feeding antenna phase distribution, and changing the matching layer towards a non-uniform topology for improved phase stability over angle.

APPENDIX

Complex permittivity extraction is achieved by fitting the measured scattering parameters S_{11}^{meas}, S_{21}^{meas} to the theoretical model of wave propagation through a dielectric slab. However, contrary to other works that involve a free-space measurement setup, the MUT is embedded in a dielectric background of relative permittivity $\varepsilon_{\text{ref}} = 9.3$. Therefore, the measured S-parameters are normalized to $Z_c = 377/\sqrt{9.3}$.

The transmission line model, similar to [9], [14], is adapted to include this dielectric background. To model S_{11}^{model}, S_{21}^{model}, we start by defining the reflection parameter Γ as

$$\Gamma = \frac{\sqrt{\varepsilon_r} - \sqrt{\varepsilon_{\text{ref}}}}{\sqrt{\varepsilon_r} + \sqrt{\varepsilon_{\text{ref}}}}. \tag{6}$$

From here, the modeled scattering parameters are a function of the independent complex variable ε_r using

$$S_{11}^{\text{model}} = \frac{\Gamma(1 - e^{-2\gamma d})}{1 - \Gamma^2 e^{-2\gamma d}}, \tag{7}$$

where $\gamma = jk_0\sqrt{\varepsilon_{\text{ref}}}$ is the complex propagation constant in the sample material, k_0 is the wave number in free space, and d is the thickness of the MUT. Similarly, the S_{21} transmission parameter can be fit using

$$S_{21}^{\text{model}} = \frac{(1 - \Gamma^2)e^{-\gamma d}}{1 - \Gamma^2 e^{-2\gamma d}}. \tag{8}$$

Next, the fitting of measurements and model is performed on phase and amplitude separately, for both the S_{11} and S_{21}. To avoid large phase errors when the amplitude of either of the two is small, weighting factors w_Γ and w_T are included for the S_{11} and S_{21}, respectively. Given the measured S-parameters $S_{11}^{\text{meas}}(f)$, $S_{21}^{\text{meas}}(f)$, the complex permittivity ε_r is obtained by minimizing the objective function

$$\min_{\varepsilon_r} \begin{bmatrix} w_\Gamma(\varepsilon_r)^2 \left(\angle S_{11}^{\text{model}}(\varepsilon_r) - \angle S_{11}^{\text{meas}}\right) \\ w_\Gamma(\varepsilon_r)^2 \left(\left|S_{11}^{\text{model}}(\varepsilon_r)\right| - \left|S_{11}^{\text{meas}}\right|\right) \\ w_T(\varepsilon_r)^2 \left(\angle S_{21}^{\text{model}}(\varepsilon_r) - \angle S_{21}^{\text{meas}}\right) \\ w_T(\varepsilon_r)^2 \left(\left|S_{21}^{\text{model}}(\varepsilon_r)\right| - \left|S_{21}^{\text{meas}}\right|\right) \end{bmatrix}, \tag{9}$$

where the weights are defined by $w_\Gamma = |S_{11}^{\text{model}}| \cdot |S_{11}^{\text{meas}}|$ and $w_T = |S_{21}^{\text{model}}| \cdot |S_{21}^{\text{meas}}|$. The function is minimized for each frequency point, using an iterative least-squares technique.

ACKNOWLEDGMENT

The authors would like to thank Ulrik Imberg from Huawei for his assistance in this project.

REFERENCES

[1] T. S. Rappaport et al., “Wireless communications and applications above 100 GHz: Opportunities and challenges for 6G and beyond,” *IEEE Access*, vol. 7, pp. 78729–78757, 2019.

[2] C.-Y. E. Tong, K. Carter, and J. Connors, “Quasi-optical characterization of low-loss polymers at 300 GHz for vacuum window applications,” *IEEE Trans. THz Sci. Technol.*, vol. 10, no. 6, pp. 713–720, Nov. 2020, doi: 10.1109/TTHZ.2020.3021352.

[3] A. Souliman, M. Kahl, D. Stock, M. Möller, B. Engel, and P. H. Bolıvár, “Defect detection in bidirectional glass fabric reinforced thermoplastics based on 3-D-THz imaging,” *IEEE Trans. THz Sci. Technol.*, vol. 13, no. 3, pp. 209–220, May 2023, doi: 10.1109/TTHZ.2023.3247609.

[4] F. Taleb, G. G. Hernandez-Cardoso, E. Castro-Camus, and M. Koch, “Characterization of building materials for THz communications,” in *Proc. 46th Int. Conf. Infrared, Millimeter THz Waves*, Chengdu, China, 2021, pp. 1–1, doi: 10.1109/IRMMW-THz50926.2021.9567176.

[5] D. K. Ghodgaonkar, V. V. Varadan, and V. K. Varadan, “Free-space measurement of complex permittivity and complex permeability of magnetic materials at microwave frequencies,” *IEEE Trans. Instrum. Meas.*, vol. 39, no. 2, pp. 387–394, Apr. 1990, doi: 10.1109/19.52520.

[6] Y. Wang et al., “Material measurements using VNA-based material characterization kits subject to thru-reflect-line calibration,” *IEEE Trans. THz Sci. Technol.*, vol. 10, no. 5, pp. 466–473, Sep. 2020, doi: 10.1109/TTHZ.2020.2999631.

[7] S. Sahin, N. K. Nahar, and K. Sertel, “A simplified Nicolson–Ross–Weir method for material characterization using single-port measurements,” *IEEE Trans. THz Sci. Technol.*, vol. 10, no. 4, pp. 404–410, Jul. 2020, doi: 10.1109/TTHZ.2020.2980442.

[8] J. Lee, M. Fujita, and M. Kim, “Characterization of antireflection absorber films using WR-3.4 waveguide fixtures,” *IEEE Trans. THz Sci. Technol.*, vol. 13, no. 5, pp. 565–568, Sep. 2023, doi: 10.1109/TTHZ.2023.3290115.

[9] D. Bourreau, A. Peden, and S. Le Maguer, “A quasi-optical free-space measurement setup without time-domain gating for material characterization in the w-band,” *IEEE Trans. Instrum. Meas.*, vol. 55, no. 6, pp. 2022–2028, Dec. 2006, doi: 10.1109/TIM.2006.884283.

[10] N. I. Lesack, N. V. Fredeen, A. Jirasek, and J. F. Holzman, “A methodology for dynamic material characterizations via terahertz time-domain spectroscopy,” *IEEE Trans. THz Sci. Technol.*, vol. 10, no. 3, pp. 282–291, May 2020, doi: 10.1109/TTHZ.2020.2972945.

[11] D. Liu, T. Lu, and F. Qi, “A reliable method for removing Fabry–Perot effect in material characterization with terahertz time-domain spectroscopy,” *IEEE Trans. THz Sci. Technol.*, vol. 10, no. 5, pp. 443–452, Sep. 2020, doi: 10.1109/TTHZ.2020.3001508.

[12] Z. Akhter and M. J. Akhtar, “Free-space time domain position insensitive technique for simultaneous measurement of complex permittivity and thickness of lossy dielectric samples,” *IEEE Trans. Instrum. Meas.*, vol. 65, no. 10, pp. 2394–2405, Oct. 2016, doi: 10.1109/TIM.2016.2581398.

[13] J. A. Hejase, E. J. Rothwell, and P. Chahal, “A multiple angle method for THz time-domain material characterization,” *IEEE Trans. THz Sci. Technol.*, vol. 3, no. 5, pp. 656–665, Sep. 2013, doi: 10.1109/TTHZ.2013.2278460.

[14] M. Mrnka, R. Appleby, and E. Saenz, “Accurate S-parameter modeling and material characterization in quasi-optical systems,” *IEEE Trans. THz Sci. Technol.*, vol. 12, no. 2, pp. 199–210, Mar. 2022, doi: 10.1109/TTHZ.2021.3140201.

[15] N. Gagnon, J. Shaker, P. Berini, L. Roy, and A. Petosa, “Material characterization using a quasi-optical measurement system,” *IEEE Trans. Instrum. Meas.*, vol. 52, no. 2, pp. 333–336, Apr. 2003, doi: 10.1109/TIM.2003.810042.

[16] G. L. Friedsam and E. M. Biebl, “A broadband free-space dielectric properties measurement system at millimeter wavelengths,” *IEEE Trans. Instrum. Meas.*, vol. 46, no. 2, pp. 515–518, Apr. 1997, doi: 10.1109/19.571899.

[17] A. Diepolder, M. Mueh, S. Brandl, P. Hinz, C. Waldschmidt, and C. Damm, “A novel rotation-based standardless calibration and characterization technique for free-space measurements of dielectric material,” *IEEE J. Microwaves*, vol. 4, no. 1, pp. 56–68, Jan. 2024, doi: 10.1109/JMW.2023.3340448.

[18] L. Dussopt, K. Medrar, and L. Marnat, “Millimeter-wave Gaussian-beam transmitarray antennas for quasi-optical S-parameter characterization,” *IEEE Trans. Antennas Propag.*, vol. 68, no. 2, pp. 850–858, Feb. 2020, doi: 10.1109/TAP.2019.2943417.

[19] A. Kazemipour et al., “Design and calibration of a compact quasi-optical system for material characterization in millimeter/submillimeter wave domain,” *IEEE Trans. Instrum. Meas.*, vol. 64, no. 6, pp. 1438–1445, Jun. 2015, doi: 10.1109/TIM.2014.2376115.

[20] L. E. R. Petersson and G. S. Smith, “An estimate of the error caused by the plane-wave approximation in free-space dielectric measurement systems,” *IEEE Trans. Antennas Propag.*, vol. 50, no. 6, pp. 878–887, Jun. 2002, doi: 10.1109/TAP.2002.1017671.

[21] S. Bosma, N. van Rooijen, M. Alonso-delPino, and N. Llombart, “A wideband leaky-wave lens antenna with annular corrugations in the ground plane,” *IEEE Antennas Wireless Propag. Lett.*, vol. 21, no. 8, pp. 1649–1653, Aug. 2022, doi: 10.1109/LAWP.2022.3176884.

[22] N. v. Rooijen et al., “A core-shell lens for antenna on-package integration at D-band,” *IEEE Trans. Antennas Propag.*, vol. 72, no. 8, pp. 6195–6208, Aug. 2024, doi: 10.1109/TAP.2024.3417628.

[23] P. F. Goldsmith, *Quasioptical Systems: Gaussian Beam Quasioptical Propagation and Applications*, Wiley-IEEE Press, 1998, pp. 9–68.

[24] C. S. Williams, “Gaussian beam formulas from diffraction theory,” *Appl. Opt.*, vol. 12, pp. 872–876, 1973.

[25] J. Bueno, S. Bosma, T. Bußkamp-Alda, M. Alonso-delPino, and N. Llombart, “Lossless matching layer for silicon lens arrays at 500 GHz using laser ablated structures,” *IEEE Trans. THz Sci. Technol.*, vol. 12, no. 6, pp. 667–672, Nov. 2022, doi: 10.1109/TTHZ.2022.3202031.

[26] Z. Hatab, M. E. Gadringer, and W. Bösch, “Propagation of linear uncertainties through multiline Thru-Reflect-Line calibration,” *IEEE Trans. Instrum. Meas.*, vol. 72, 2023, Art. no. 1007409, doi: 10.1109/TIM.2023.3296123.

[27] Z. Hatab, M. Gadringer, and W. Bösch, “Improving the reliability of the multiline TRL calibration algorithm,” in *Proc. 98th ARFTG Microw. Meas. Conf.*, Las Vegas, NV, USA, 2022, pp. 1–5, doi: 10.1109/ARFTG52954.2022.9844064.

NICK VAN ROOIJEN received the M.Sc. degree *(cum laude)* in electrical engineering from the Delft University of Technology (TU Delft), Delft, The Netherlands, in 2021, where he is currently working toward the Ph.D. degree with Terahertz Sensing Group. He worked on a first-time demonstration of a high frequency scanning-lens phased-array during his master’s degree. His research focuses on the development of a Fly’s eye lens array for high frequency communication applications, including the analysis, design, and measurement of integrated lens antennas and leaky-wave structures. Mr. van Rooijen was the co-recipient of the Best Theory And Design Antenna Paper Award and was also nominated for the Best Applied Technology Antenna Paper Award, both at the 16th European Conference on Antennas and Propagation (EuCAP) in 2022.

MARIA ALONSO-DELPINO (Senior Member, IEEE) received the degree in telecommunications engineering from the Technical University of Catalonia (UPC), Barcelona, Spain, in 2008, the M.S. degree in electrical engineering from the Illinois Institute of Technology, Chicago, IL, USA, in 2008, and the Ph.D. degree in signal theory and communications/electrical engineering from UPC in 2013. From 2014 to 2015, she was a Postdoctoral Researcher with the Delft University of Technology (TU Delft), Delft, The Netherlands. From 2015 to 2016, she was a NASA Postdoctoral Fellow with Jet Propulsion Laboratory (JPL), Pasadena, CA, USA. From 2016 to 2020, she was a Member with the Technical Staff with the Sub-millimeterWave Advanced Technology Group of JPL/NASA. Since 2020, she has been an Assistant Professor with TU Delft. Her research interests include millimeter- and submillimeter-wave heterodyne and direct detection receiver technologies, antennas, and quasi-optical systems. Dr. Alonso-delPino was the recipient of the 2014 IEEE Terahertz Science and Technology Best Paper Award and the recipient of the Outstanding Reviewer Award of IEEE TRANSACTIONS ON TERAHERTZ SCIENCE AND TECHNOLOGY in 2013, has been nominated in 2021, 2022, and 2024, for Best papers at the European Conference on Antennas and Propagation (EuCAP), and the Best Antenna Design Paper Award in 2022, and the IETE-Smt C Ranganayakamma Memorial Award in 2024. Since 2024, she has been a Regional Delegate of European Association on Antennas and Propagation (EurAAP) of Region 5 Netherlands, Belgium, Luxemburg.

NURIA LLOMBART (Fellow, IEEE) received the master's degree in electrical engineering and the Ph.D. degree in electromagnetics from the Polytechnic University of Valencia, Valencia, Spain, in 2002 and 2006, respectively. During her master's degree studies, she spent one year with the Friedrich Alexander University of Erlangen Nuremberg, Erlangen, Germany, and was with the Fraunhofer Institute for Integrated Circuits, Erlangen, Germany. From 2002 to 2007, she was with the Antenna Group, TNO Defense, Security and Safety Institute, The Hague, The Netherlands, working as a Ph.D. degree Student and afterward as a Researcher. From 2007 to 2010, she was a Postdoctoral Fellow with the SubmillimeterWave Advance Technology Group, Jet Propulsion Laboratory, California Institute of Technology, Pasadena, CA, USA. From 2010 to 2012, she was a "Ramón y Cajal" Fellow with the Optics Department, Complutense University of Madrid, Madrid, Spain. In 2012, she was with the THz Sensing Group, Technical University of Delft, Delft, The Netherlands, where she has been a Full Professor since 2018. She has coauthored more than 200 journal and international conference contributions in the areas of antennas and terahertz systems. Dr. Llombart was the corecipient of the H. A. Wheeler Award for the Best Applications Paper of 2008 in IEEE TRANSACTIONS ON ANTENNAS AND PROPAGATION, 2014 THz Science and Technology Best Paper Award of the IEEE Microwave Theory and Techniques Society, and several NASA awards. She was also the recipient of the 2014 IEEE Antenna and Propagation Society Lot Shafai Mid-Career Distinguished Achievement Award, European Research Council Starting Grant in 2015. She is a Board Member of the International Society of Infrared, Millimeter, and Terahertz Waves and, has been the Editor in Chief of IEEE TRANSACTIONS ON TERAHERTZ SCIENCE AND TECHNOLOGY since 2023. In 2019, she was appointment IEEE Fellow for contributions to millimeter and submillimeter wave quasi-optical antennas.